Atmos. Chem. Phys., 13, 1293–1310, 2013
www.atmos-chem-phys.net/13/1293/2013/
doi:10.5194/acp-13-1293-2013

Atmospheric Chemistry and Physics Open Access

Aerosol properties over Interior Alaska from lidar, DRUM Impactor sampler, and OPC-sonde measurements and their meteorological context during ARCTAS-A, April 2008

D. E. Atkinson[1,2,*], K. Sassen[2,3], M. Hayashi[4], C. F. Cahill[3,6], G. Shaw[3,5], D. Harrigan[7], and H. Fuelberg[7]

[1]International Arctic Research Center, University of Alaska Fairbanks, 930 Koyukuk Drive, Fairbanks, Alaska, 99775, USA
[2]Department of Atmospheric Sciences, University of Alaska Fairbanks, 930 Koyukuk Drive, Fairbanks, Alaska, 99775, USA
[3]Geophysical Institute, University of Alaska Fairbanks, 903 Koyukuk Drive, Fairbanks, Alaska, 99775, USA
[4]Department of Earth System Science, University of Fukuoka, 8-19-1 Nanakuma, Jonan-ku, Fukuoka 814-0180, Japan
[5]Department of Physics, University of Alaska Fairbanks, P.O. Box 755920, Fairbanks, AK 99775-5920, USA
[6]Department of Chemistry, University of Alaska Fairbanks, P.O. Box 755920, Fairbanks, AK 99775-5920, USA
[7]Department of Meteorology, The Florida State University, Dept. of Meteorology/404 LOV, 1017 Academic Way/ P.O. Box 3064520, Tallahassee, FL 32306-4520, USA
[*]present address: Department of Geography, University of Victoria, P.O. Box 3060 STN CSC, Victoria, BC, V8W 3R4, Canada

Correspondence to: D. E. Atkinson (datkinso@uvic.ca)

Received: 20 April 2011 – Published in Atmos. Chem. Phys. Discuss.: 10 June 2011
Revised: 11 December 2012 – Accepted: 14 December 2012 – Published: 1 February 2013

Abstract. Aerosol loading over Interior Alaska displays a strong seasonality, with pristine conditions generally prevailing during winter months. Long term aerosol research from the University of Alaska Fairbanks indicates that the period around April typically marks the beginning of the transition from winter to summer conditions. In April 2008, the NASA-sponsored "Arctic Research of the Composition of the Troposphere from Aircraft and Satellites" (ARCTAS) field campaign was conducted to analyze incursions of aerosols transported over Alaska and the Canadian North. In and around Fairbanks, Alaska, data concerning aerosol characteristics were gathered by polarization (0.693 µm) lidar, DRUM Impactor sampler, and balloon-borne optical particle counter. These data provide information on the vertical distribution and type of aerosol, their size distributions, the chemical nature of aerosol observed at the surface, and timing of aerosol loading. A detailed synoptic analysis placed these observations into their transport and source-region context. Evidence suggests four major aerosol loading periods in the 25 March–30 April 2008 timeframe: a period during which typical Arctic haze conditions prevailed, several days of extremely clear conditions, rapid onset of a period dominated by Asian dust with some smoke, and a period dominated by Siberian wildfire smoke. A focused case study analysis conducted on 19 April 2008 using a balloon-borne optical particle counter suggests that, on this day, the majority of the suspended particulate matter consisted of coarse mode desiccated aerosol having undergone long-range transport. Backtrack trajectory analysis suggests aged Siberian wildfire smoke. In the last week of April, concentrations gradually decreased as synoptic conditions shifted away from favoring transport to Alaska. An important result is a strong suggestion of an Asian dust incursion in mid-April that was not well identified in other ARCTAS measurements. The lidar and OPC-sonde unambiguously discern aerosols height stratification patterns indicative of long range transport. Identification of a dust component is suggested by DRUM sampler results, which indicate crustal species, and supported by synoptic and trajectory analysis, which indicates both a source-region lifting event and appropriate air-mass pathways.

Published by Copernicus Publications on behalf of the European Geosciences Union.

1 Introduction

Transport of aerosols is of particular concern in the Arctic because transportation from remote locations can be a primary source for contaminants that would not otherwise be observed. Various researchers have addressed aspects of this topic. Stohl et al. (2007) provide an excellent overview of some of the problems associated with aerosol transport to the Arctic. Following a distant biomass burning episode, they noted atmospheric contaminants which included ozone, carbon monoxide, and gaseous elemental mercury in the European and Russian Arctic (Stohl et al., 2007). Enhanced deposition can be found on snow surfaces. In these cases the surface radiation balance can be altered by a reduction of albedo, which can act to hasten seasonal melt (Stohl et al., 2007; Haywood and Boucher, 2000). Douglas and Sturm (2004) identify various trace contaminants, including lead and cadmium, in the snow along a transect extending across northern Alaska. In terms of source attribution for observed surface contaminants, several studies have noted a link between the occurrence of atmospheric or surface contaminants and the timing of Arctic Haze events. For example, the contamination noted by Douglas and Sturm (2004) was observed to increase in the late winter, which they found to correspond to atmospheric haze loading.

Key to interpreting local observations of contaminant/aerosol loading is an understanding of the meteorological context. This establishes aerosol trajectory and aids identification of source regions, which helps explain why specific aerosols are being observed. Several of the studies mentioned above sought to identify source regions using meteorological and/or air mass trajectory analysis (Stohl et al., 2007; Polissar et al., 1999; Halter et al., 1985). In support of the ARCTAS project, Fuelberg et al. (2010) performed a comprehensive analysis in which source regions and pathways were identified for the entire Arctic north of 60° north latitude.

In recent years, trends in global environmental change have exerted a particularly strong impact on the Arctic (ACIA, 2005). As indicated by the sample of literature discussed above, it is clear that the Arctic is affected, from both a contaminant and a radiation balance perspective, by aerosol emissions from more southerly latitudes, including wildfires and industrial sources. It is also clear that more work is required on various aspects of the topic. Thus, to provide a better overall understanding of this phenomenon over Alaska, the Canadian Arctic Archipelago, and adjacent waters, in April 2008 the NASA project, "Arctic Research of the Composition of the Troposphere from Aircraft and Satellites" (ARCTAS) was conducted. The ARCTAS project consisted of an intensive field campaign that included five research aircraft (NASA, NOAA, Department of Energy, National Research Council of Canada) and ground based in situ and remote-sensing instruments, operated by researchers from more than 40 universities and government laboratories. One specific objective of the ARCTAS project was to examine long-range transport of pollutants to the Arctic (Jacob et al., 2010) during the period when pollutant concentrations are greatest, termed "arctic haze" events (Shaw, 1995).To provide optimal opportunity for capturing haze events, the field campaign was conducted during the mid-spring period. In particular, ARCTAS was focused on boreal fire emissions, their injection, transport, composition, and radiative effects. Jacob et al. (2010) discuss in detail the overall project rationale, design, discharge, and some major results. This paper focuses on description and analysis of ground- and balloon-based observations gathered over Interior Alaska, and the meteorological context during the observing period, for the first phase of the mission, ARCTAS-A.

This paper has three main objectives:

1. Identify major aerosol events over Interior Alaska as manifested in the data obtained by the ground-based instruments.

2. Determine relative loading contributions as smoke vs crustal/mineral sources.

3. Examine the meteorological controls in place during the identified aerosol events that governed episodes of long-range aerosol transport into the region and assess whether observations during ARCTAS may be considered typical.

Fuelberg et al. (2010) ("F10" hereafter) review the climatological context and indicate how the 30 March to 22 April 2008 period differed from climatology, and they provide a comprehensive assessment of mean atmospheric state during the mission timeframe. In particular, F10 indicate notable climatological departures from normal, including a northerly displacement of the North Pacific jet and a corresponding more northerly cyclone pathway, leading to cyclolysis over Northern Alaska. F10 document a subtropical anticyclone that is stronger and displaced farther to the north than normal, which explains the northward shifted jet and stormtracks. F10 also indicate enhanced cyclonic activity in the Lake Baikal region of southeastern Siberia, north of the border with Mongolia. This paper builds upon the meteorological results of F10 by examining the implications of the climatic anomaly on transport to the Interior Alaska region in terms of a detailed synoptic and trajectory analysis.

2 Data and methods

2.1 Ground-based and profile observations

At several locations in the Alaska Interior (Fig. 1), three ground-based in situ and remote sensing instruments were operated during the ARCTAS-A experiment: two that performed direct aerosol sampling – one ground-based DRUM Impactor sampler and one balloon-launched optical particle

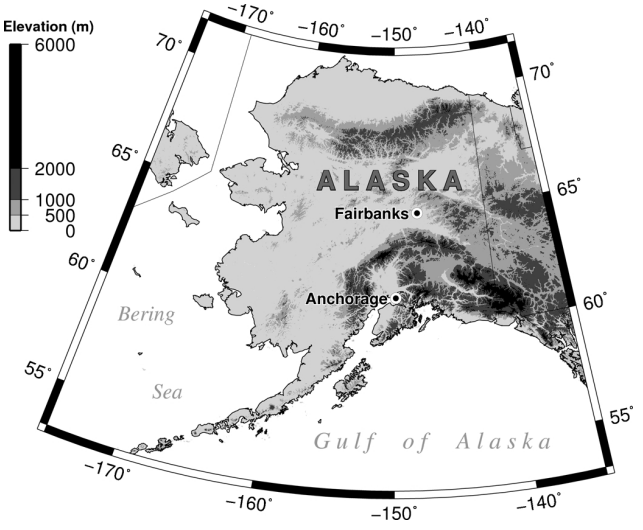

Fig. 1. Alaska showing the topographic context of Fairbanks and the Alaska Interior. Surface data were obtained at locations in Fairbanks or at the Poker Flat Research Range, 50 km northeast of Fairbanks. The Alaska Mountain Range is between Fairbanks and Anchorage.

counter sampler – and one ground-based cloud polarization lidar system. These instruments were situated (or launched) in and within 50 km of the city of Fairbanks (Fig. 1) and provided the data used in this analysis. The DRUM Impactor and lidar were operated throughout April, and the balloon-borne optical particle counter was used to perform a focused case-study on one day (19 April).

2.1.1 Arctic Facility for Atmospheric Remote Sensing (AFARS)

The Arctic Facility for Atmospheric Remote Sensing (AFARS) is located on the University of Alaska Fairbanks campus (64.86° N and −147.84° W, at 286 m above mean sea level – a.m.s.l.). At this facility, active since 2004, is operated a "turnkey" Cloud Polarization Lidar (CPL). The high-power (1.5 J) CPL collects polarization measurements at a wavelength of 0.694 µm using a pulse repetition rate of 0.1 Hz (Sassen and Khvorostyanov, 2008). CPL linear depolarization ratios (see below) are accurate to about ±0.02 for the range of aerosol values reported here.

Depolarization measurements are computed using the backscatter from linearly-polarized transmitted laser light by determining the ratio of the backscattered power (β) in two of the orthogonal polarization planes (P) relative to that transmitted, as a function of range (R). For simple two-channel polarization lidars, the "total" linear depolarization ratio is defined by

$$\delta = \frac{P(R)_{\perp}}{P(R)_{||}} = \frac{[\beta_{\mathrm{m}}(R)_{\perp} + \beta_{\mathrm{a}}(R)_{\perp} + \beta_{\mathrm{c}}(R)_{\perp}]}{[\beta_{\mathrm{m}}(R)_{||} + \beta_{\mathrm{a}}(R)_{||} + \beta_{\mathrm{c}}(R)_{||}]} \quad (1)$$

where the subscripts m = molecular, a = aerosol, and c = cloud represent the contributions to backscattering from each atmospheric species category. Although the relatively strong backscattering from clouds normally dominates the total signal, a mixture of molecules and aerosols can produce intermediate δ values between the value typical of the pure molecular atmosphere ($\delta \approx 0.03$ with the CPL) and that value characteristic of the aerosol species. "Total signal" refers to the combination of the backscattered signals from both the aerosol and air molecules (which produce only a slight depolarization). This means that the presence of a depolarizing aerosol in the column has an effect on δ, as a function of the aerosol concentration. Thus, the measured depolarization from an aerosol-air mixture depends on the size and concentration of the aerosols and the air pressure (i.e., height). Time averaged δ values are used in this study, which are determined using the summed returned signals in each channel at each height. A 10-min averaging period was used to reduce the influence of noise.

The polarization lidar technique (Sassen, 2000, 2005a) has the unique ability to discriminate between spherical and nonspherical particles in the atmosphere, and thus determine unambiguously the thermodynamic phase of clouds. Furthermore, its sensitivity to particle shape can often facilitate identification of atmospheric aerosol type. Spherical aerosols (e.g., haze and aqueous smoke particles) produce little or no change in the polarization state of backscattered light, whereas nonspherical particles, like dust, can generate considerable depolarization depending on the exact particle shape and, to some extent, on the particle size relative to the incident wavelength (Mishchenko and Sassen, 1998). If the particle dimensions are smaller than the incident wavelength, reduced depolarization will be measured for a particular nonspherical particle due to the effects of the onset of Rayleigh scattering. For example, dust storm aerosols are relatively large and have a highly irregular shape, and typically generate δ of about 0.25 to 0.35, which is similar to many cirrus ice crystal clouds. Intermediate (and increasing) δ are found for aged (i.e., crystallized) sulfate haze and smoke aerosol, forest fire ash, tree pollen, and volcanic ash (Sassen, 2008). Fresh smoke aerosol sampled in Alaska (Sassen, 2008; Sassen and Khvorostyanov, 2008) typically generate near-zero δ (i.e., < 0.03), but during transport under dry conditions aged smoke can produce values in the 0.05–0.10 range (Murayama et al., 2004). The phenomenon of increasing δ with particulate age occurs as the aerosol loses its moisture coating, exposing the irregular aerosol surface (Sassen et al., 1989), while dry or wet (from cloud processing) particle coagulation could also lead to this result. On the other hand, local moist conditions could reactivate hygroscopic nuclei into haze particles, which produce near-zero δ. While aerosols can cycle between gaining a moisture coating and desiccation repeatedly during transport, which is a function of the local RH along the transport path, the point here is that fresh smoke would have near-zero δ, which means that,

if it is suspected the sampled layer contains smoke, an elevated δ means that it is most likely not locally sourced.

During the ARCTAS period at AFARS, a total of 20, 1- to 2-h data acquisition sessions were conducted with the CPL between 1 April and 1 May 2008. Observation timing was geared principally to coincide with afternoon overpasses of the A-train satellite formation and local ARCTAS-NASA aircraft flight activities. Data collection was not attempted during periods of low cloud and snowfall that would effectively block the lidar measurements.

2.1.2 DRUM Impactor sampler

A three-stage DRUM Impactor sampler system is operated at the Poker Flat Research Range (e.g., Cahill, 2003). This instrument samples aerosols over a range of sizes. For each chemical species, total mass is measured and relative concentrations are calculated for the different size cuts represented by each stage (Raabe et al., 1988). The sampling inlet is a standard PM_{10} inlet connected to a $PM_{2.5}$ cyclone. Each DRUM strip has mylar before and after and to the sides of the sample deposit that are suitable for use as a blank. Clean mylar is used before the start and after the stop of the sample deposit to determine the blank for the sample. The laboratory is also equipped with blanks that are used to confirm the quality of the mylar and Apiezon coating. A zero air test was not explicitly conducted because this only results in a field blank (a sample which did not have air impacted upon it) and there is already a field blank, mentioned above, for every sample strip collected. In the laboratory during sample preparation, the sample strips only touch surfaces that have been thoroughly cleaned with laboratory grade propanol. The samples are then loaded into sample transport cups until they are installed in the sampler, which was cleaned before its use in this experiment. In general, all DRUM analyses use the protocols of DRUM Quality Assurance: protocols, latest version DQAP ver 1/09, on the UC Davis DELTA Group web site http://delta.ucdavis.edu. These protocols have been accepted by the US EPA in Joint QA/QC protocols in the recent EPA NEXUS study in Detroit.

The field situation of the instrument is in the second story of a building that received almost no visitation during the sampling period. The building is located on the top of a hill at the Poker Flat Research Range, 50 km NE of the only population center in the area. The few local emission sources that exist in the local vicinity are small and below the inversion layer that forms in the bottom of the valley below the hill. The sampling was not sector controlled because there are no upwind sources in any direction to be concerned about. The DRUM sampler was operated continuously between 25 March and 30 April 2008 with a temporal resolution of 3 h.

After field collection, the aerosol samples are analyzed using Synchnotron X-Ray Flourescence (Cahill et al., 1999) for species identification. The x-ray analysis was performed at Lawrence Berkeley National Laboratory's Advanced Light Source. The samples were stored on slide frames in sample storage boxes designed to hold these samples. The boxes were kept in a clean laboratory at room temperature. Previous experience with DRUM samples showed that they are stable under these storage conditions (including sulfuric acid aerosols). The samples were analyzed approximately seven months after collection (the first available analysis run after the sample collection). For this study the chemical species most broadly related to forest fire and haze (K and S) and mineral dust/industrial activity (Ca, Si and Fe) in a single size category (0.34–1.15 µm) are analyzed.

2.1.3 Balloon-borne particle sampler

In-situ sampling of aerosols in the vertical profile over Fairbanks was conducted using a balloon-borne, step-integrating optical particle counter (an "OPC sonde"). A standard weather balloon conveys the sonde, built by Yamanashi Gijutu Kobou Co. Ltd. and Meisei Electric Company of Japan. The OPC samples environment air with a flow rate of 3 L min^{-1} (50 cm^3 s^{-1}) through a stainless inlet pipe with diameter of 5.0 mm and length of 10 cm. The instrument detects light scattered by aerosol particles ingested in the inlet stream using a scattering angle of 60 degrees and the half solid angle collection field of 39.2 degrees. The instrument counts electric pulses larger than pre-set threshold intensities, corresponding to spherical particle diameters in eight size categories: 0.3, 0.5, 0.8, 1.2, 2.0, 3.4, 5.0, and 7.0 µm with refractive index of 1.40–0i. Calibration of intensity was performed using standard size Polistylen latex spheres, refractive index of 1.59–0i. Threshold values for particles of refractive index 1.40–0i were determined using Mie scattering theory. Pulse data are accumulated for 16 s, corresponding to 80 m of vertical resolution, and are then transmitted to a ground station. No dilution system was used. The OPC sonde also returns temperature, humidity, and winds via GPS tracking. In addition to aerosol counts, housekeeping data were returned by the unit that monitored the state of the OPC system throughout its sampling run, including conditions of the pump and laser diode.

Quality checks of optical response for standard size polistylen Latex particles and flow rate were performed before launch and after recovery following the profile observation. Zero filter air checks were also performed just before launch and just after recovery. This instrument has been successfully used in support of many other campaigns (e.g., Iwasaki et al., 2007; Hayashi et al., 1998) and is described in greater detail in Iwasaki et al. (2007).

2.2 Meteorological data and analysis methods

Data to perform the meteorological assessment are drawn from the reanalysis datasets held at NOAA's Earth System Research Laboratory. The NCEP/DOE Global reanalysis (NNR) dataset (Kalnay et al., 1996), developed at NOAA's

National Centers for Environmental Prediction in conjunction with the National Center for Atmosphere Research (NCEP/NCAR), is used for this study. The NNR dataset possesses a spatial resolution of 2.5 degrees latitude and longitude, temporal resolution of 6 h, and is useful for establishing broad features of the large scale flow and, in particular, anomaly patterns. The NOAA/ESRL on-line plotting and analysis tool (http://www.esrl.noaa.gov/psd/data/composites/hour/) is used to prepare plots of meteorological variables.

The reanalysis data are used to identify general atmospheric flow patterns to better understand the instrumental observations. This was based on geopotential height charts at 925, 850, and 700 hPa. The 925 hPa level is used to represent the near-surface flow. The 850 and 700 hPa levels are used to assess flow that corresponds to the heights of some of the features observed in the CPL or OPC sonde data. Where useful, wind and temperature data are mentioned. To further assist in source-region interpretation and attribution, forward- and back-trajectory analyses are conducted by Harrison and Fuelberg using a Lagrangian particle dispersion model, "FLEXPART", as applied to a gridded Northern Hemisphere wind and pressure data set generated by operating the Weather and Research Forecast (WRF) modeling system (F10).

3 Results

3.1 CPL

Weather permitting, CPL data were gathered almost every day over the 1 to 30 April period. On several days the lower atmosphere was blocked to lidar probing by snowfall and low clouds. For this reason a subset of days is selected for presentation. This amounts to roughly one 2–3 h data collection period every 3–5 days, that allows for the most thorough analysis and that provides a reasonably well distributed sampling spread over the analysis period (Fig. 2). The days selected for presentation are 4, 9, 13, 15, 21, and 24 April. The CPL is occasionally recalibrated, however basic uncertainties and slow drifts in errors remain. Despite this, over short periods the relative differences in depolarization have meaning in helping to identify aerosols despite any small bias in the values.

The afternoon of 4 April (Fig. 2a) shows only a weakly-backscattering boundary layer aerosol beneath a bright, $\sim$7.0–10.0 km high cirrus cloud layer generating $\delta \approx 0.5$. The top of the boundary layer, identified at $\sim$3.0 km a.m.s.l., is sporadically marked by ice scud clouds composed of horizontally oriented plate crystals, which can generate near-zero depolarization. Only a weak decline in signal is evident aloft as the laser pulse exits the diffuse haze layer. Although, near the surface, average $\delta \approx 0.07$ is present, it decreases to 0.02–0.03 higher in the boundary layer. The larger backscatter value at low-levels suggests a combination of urban pollution and weak Arctic haze in the boundary layer. CPL observations of low-level, depolarizing returns are common in winter in Fairbanks as local pollution gets trapped in strong surface inversions. By 9 April (Fig. 2b), a boundary layer up to $\sim$1.5 km a.m.s.l. is apparent as a brighter zone in the backscatter and stronger depolarization signal. After 23:00 UTC scud is beginning to form at the top of the boundary layer. Above the boundary layer, the profile is showing greater backscatter and some vertical structure in the form of a distinct layer at $\sim$3 km a.m.s.l. Polarization values are elevated, indicating non-spherical particles.

The 13 April data (Fig. 2c) indicate mid-level altostratus cloud ($\sim$6–7 km a.m.s.l.) that is dominated by ice and occasionally contains oriented ice plates, as well as a supercooled ($\sim -22\,^{\circ}$C) altocumulus cloud at $\sim$4.5 km a.m.s.l. (indicated by the bright, low-δ layer at around 21:00 UTC). In addition to the boundary layer Arctic haze ($\delta \approx 0.04$), a thin elevated aerosol layer is present at $\sim$2.5 km a.m.s.l. with $\delta \approx 0.07$ before it disappears into the descending cloud base. This level of depolarization indicates nonspherical particles, either too diffuse or small to generate higher δ, and corresponds to a dry air layer often associated with transported Asian dust or smoke layers (Iino et al., 2004).

By early 15 April (Fig. 2d), the aerosol signal is stronger and extends well into the broken cirrus layer from 5.5–8.0 km a.m.s.l. Backscatter patterns show stratification into fine horizontal layers, a common observation associated with long-range transport (e.g., Müller et al., 2005; Mariano et al., 2010). Low values for δ ($\sim$0.02) are present near the surface, which increase to 0.07 in some of the aerosol layers (e.g., at 3.7 km), again suggesting a vertical gradient in spherical and nonspherical particles.

The data for the afternoon of 21 April (Fig. 2e) reveal a shift to still more strongly backscattering and depolarizing aerosols. The aerosol is indicated to extend up to at least $\sim$7.0 km a.m.s.l., and there is a layer of enhanced backscattering at 4.5 km a.m.s.l. with $\delta \approx 0.09$ that seems related to aerosol processing in an evaporating cirrus cloud fallstreak observed prior to 21:00 UTC. CPL depolarization in the near-surface aerosol layers ranges from 0.04–0.06. The final CPL displays for 24 April (Fig. 2f) again reveal a layered aerosol structure beneath cirrostratus cloud: the lower layer yields average $\delta = 0.05$, while the layer aloft at $\sim$4.0 km a.m.s.l. generates δ of 0.15, the highest values noted during the ARCTAS period.

Thus, overall, the CPL results suggest a sequence of events based on atmospheric loading patterns that are distinguished by the relative strength of the backscattering, depolarization, and/or depths and structures of the aerosol returns. The early April period begins with low-loading conditions. Near the surface, returns can be interpreted as a mixture of diffuse Arctic haze and low-level urban pollution from the adjoining Fairbanks area. An interpretation of local pollution in the lower layers is suggested for two reasons: the strongest returns are confined to the boundary layer, and the backscatter

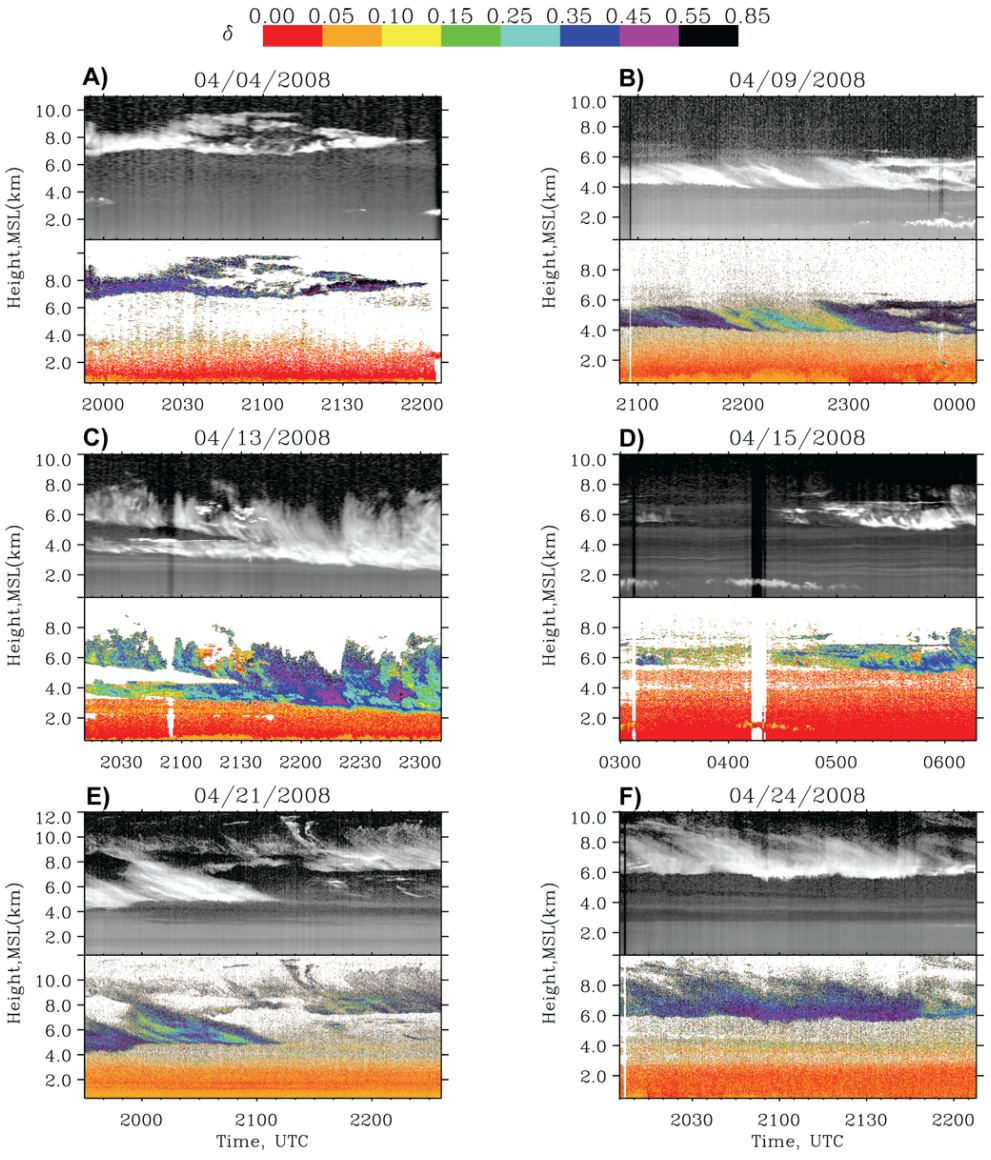

Fig. 2. AFARS lidar height-time display plots of the evolution of troposphere cloud and aerosol conditions during the ARCTAS campaign; the best six plots were selected to be spaced relatively evenly throughout the month of April. Each plot contains two images: the upper image shows relative returned (attenuated) lidar backscatter power in terms of a logarithmic gray scale (where white is the strongest range-normalized signal); the lower image shows lidar linear depolarization ratio (δ) (note color scale at top of figure). All displays start at an altitude of 0.5 km a.m.s.l. because signals are unreliable in the first 200 m or so due to incomplete laser/receiver overlap. White areas in the depolarization displays have insufficient signals to calculate delta. Time values are in UTC, and the date of lidar data collection period is at the top of each image; in the text they are referred to as: **(A)** 4 April; **(B)** 9 April; **(C)** 13 April; **(D)** 15 April; **(E)** 21 April; **(F)** 24 April. An additional set of lidar data are available for 19 April, which and are presented in Fig. 8.

does not exhibit the layering that is associated with long-range transport of aerosol. At some point before 9 April a large influx of non-spherical, non-locally derived aerosol occurs. A relatively high δ suggests desiccated dust or aged smoke. The amount of aerosol in the atmosphere decreases gradually over the next two CPL data collection periods, to some point past 15 April, as indicated by the weakening backscatter strength. Polarization also decreases but the fine layering patterns become more pronounced, continuing to indicate long-range transport. At some point before 21 April another large influx of non-spherical, non-locally derived aerosol occurs, with atmospheric loading characteristics persisting past 25 April. Again, long-range transport is suggested by the layering, and again polarization has increased, suggesting desiccated dust and/or aged smoke.

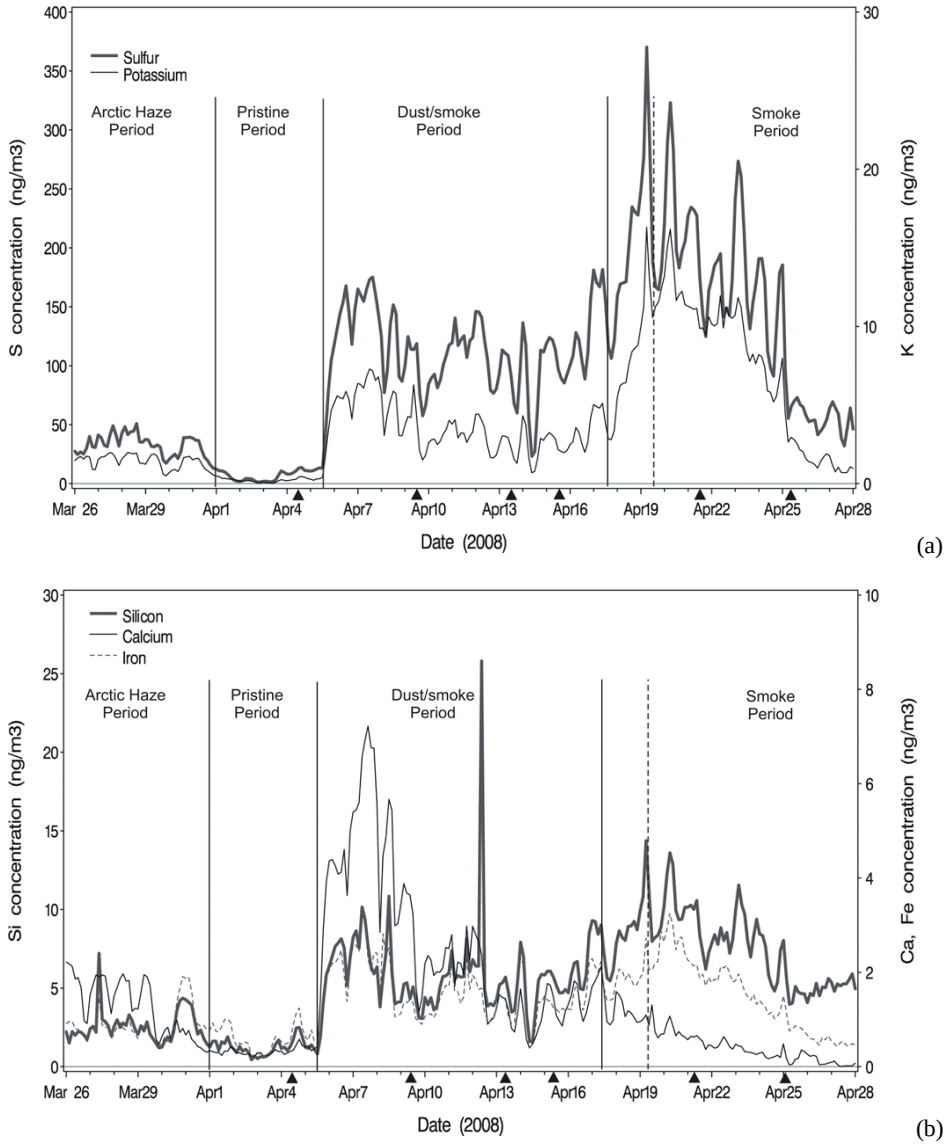

Fig. 3. DRUM Impactor sampler species traces: **(a)** wildfire species (S, Ca); **(b)** mineral (Si, K) and industrial species (Fe). Sampled size fraction: 0.1 to 0.34 µm. Times of CPL data gathering periods (black triangles) and the day of the OPC balloon-sonde (vertical dashed line) are indicated. The aerosol periods identified in the Discussion are also separated by the thin vertical lines. Minimum detectable limits are as follows (ng m^{-3}): S: 3.1, Ca: 0.3, Fe: 0.4, Si: 2.6, K: 0.6.

3.2 DRUM Impactor sampler results

Time series traces of five chemical species are presented: S and K, often associated with wildfire (Yamasoea et al., 2000; Cahill et al., 2008, Fig. 3a); Si and Ca, often associated with mineral sources (Chiapello et al., 1997, Fig. 3b); and Fe, a standard industrial tracer (Malm et al., 1994; Fig. 3b). During the timeframe of measurement, the winds at the site were predominantly calm; thus, wind effects on the inlet should not cause any sampling bias. The absolute humidity and temperature at the site during the sampling period were measured and were low, so although the samples were collected at ambient temperature, they were basically dry. All of the aerosol chemical mass concentrations obtained were low, with many element concentrations ranging below minimum detectable limits (which are noted in the caption for Fig. 3). This was not instrument error; concentrations were simply low. The period immediately preceding the start of the experimental timeframe had an extraordinarily low atmospheric aerosol loading, a fact that was supported by visual inspection of the sky and distant objects. For this early time period coincident measurements of the same species at larger size fractions, not shown, all indicated lower concentrations than the smallest size fraction presented here. This is consistent with larger particles settling out during transport and smaller particles growing into accumulation mode

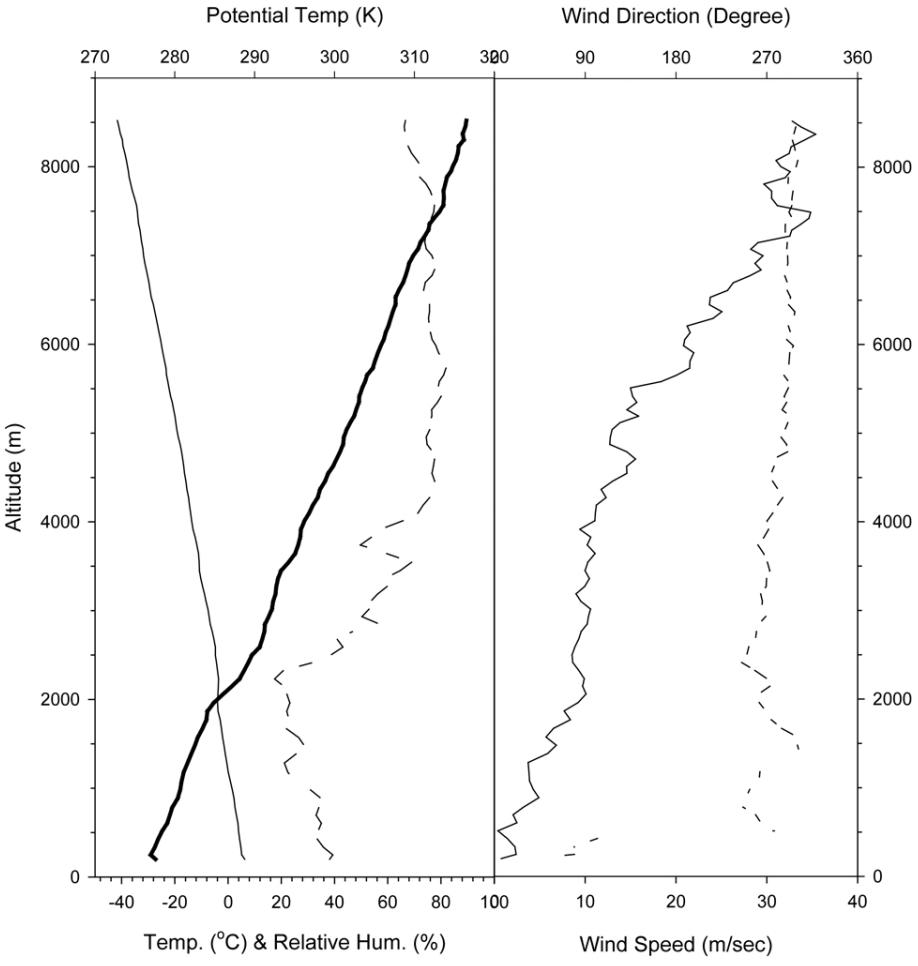

Fig. 4. Vertical profiles of meteorological parameters measured by the OPC sonde, 19 April 2008. **(a)** Temperature (thin line), potential temperature (heavy line), and humidity (dashed line), and **(b)** wind speed (solid line) and direction (dashed line) profiles observed with meteorological sonde.

sizes through coagulation and gas-to-particle conversion during transport (Seinfeld and Pandis, 2006), although it must also be noted that initial emission may have simply included lower concentrations at the larger size fractions. The broad patterns indicated in Fig. 3a and b may be summarized as follows: a first, early period of low concentrations, the latter part of which is the only time during which Fe exceeds Ca; a second period of very low concentrations for all species; a third period of rapid-onset large concentration increases for all species, in which Ca responds with particular strength; and a fourth and final period characterized by large increases in concentrations for wildfire species (K and S).

3.3 OPC

The OPC balloonsonde was launched at Fairbanks at 22:00 UTC, 19 April and gathered aerosol size distribution data continuously from 198 m up to 8500 m, after which the balloon disintegrated and the OPC unit returned to earth for recovery. Size distributions were measured from 0.3 to 7.0 µm in diameter. Size criteria were calibrated against a refractive index of 1.4–0i. Background atmospheric conditions consisted of, at the surface, calm winds with a moderate humidity of $\sim$ 40 %. Wind speed increased gradually with height, reaching $\sim 15\,\mathrm{m\,s^{-1}}$ by 4000 m, and settled on a consistent west-northwesterly direction. Between 1 and 2.2 km the atmosphere was very dry (Fig. 4). The lower levels of the atmosphere were very stable, as inferred from radiosonde data (not shown), and similar conditions existed in the days leading up to 19 April. This suggests that minimal contribution is to be expected from Fairbanks' urban sources to the aerosol load observed above the strong diurnal inversion layer because the launch took place away from town.

Vertical profiles of size distributions for the eight aerosol size fractions returned by the OPC indicated the presence of discernible layers (Fig. 5). In general, total aerosol loading in the lowest 4.1 km was relatively high, approaching 100 particles $\mathrm{cm^{-3}}$ even in the free troposphere up to

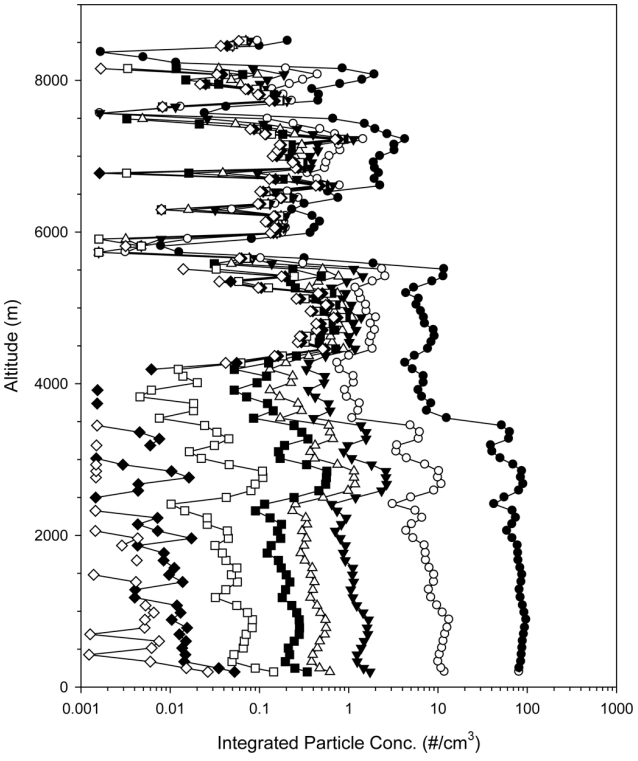

Fig. 5. Vertical profiles of aerosol concentration for eight size criteria observed with the OPC sonde, 19 April 2008. The horizontal axis represents the total number concentration larger than each size criteria shown in the legend.

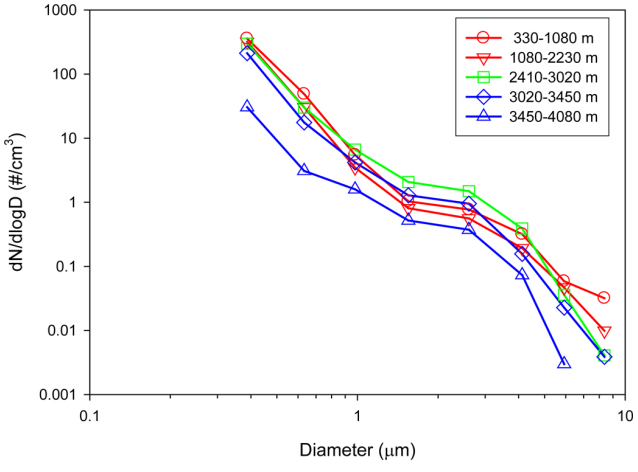

Fig. 6. Number size distributions in classified layers below 4.1 km. Data obtained from the OPC sonde, 19 April 2008.

3.5 km, with a reduction to ∼ 50 particles cm^{-3} above 3.5 km (Fig. 6). When broken down by size fraction, counts exhibited strong differences. Counts for the two largest size fractions are very low, decreasing up the profile from a maximum at the surface. Counts for the mid-range sizes – ∼ 1 µm – were relatively low, and counts for the finer size fractions and

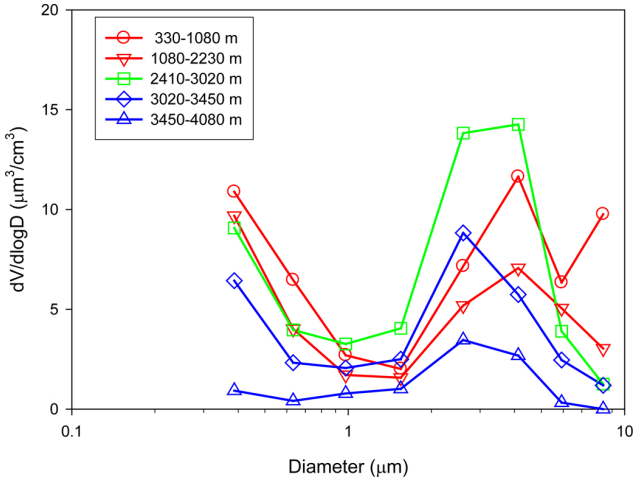

Fig. 7. Volume size distributions in classified layers below 4.1 km. Data obtained from the OPC sonde, 19 April 2008.

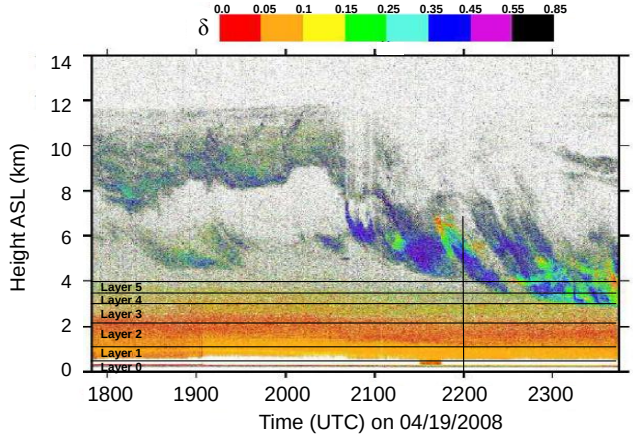

Fig. 8. Lidar depolarization ratio display collected on 19 April 2008 bracketing the OPC balloon-sonde launch (note vertical line at 22:00 UTC). Layers defined in the text are marked and labeled. The vertical line at 22:00 h is the time of the OPC-sonde launch.

the 2 and 5 µm size fraction range were higher (Fig. 6), with counts in the smallest size fractions (60–240 nm) highest at least for the level of measurement, around ∼ 500 m a.s.l. (Fig. 7).

The most readily noticeable layer feature is the transition that occurs above 4.1 km. In this layer the largest size fractions exhibit a rapid increase in concentration, indicating that the OPC penetrated an ice cloud. In this case, the OPC is counting ice crystals as large aerosols, which explains the rise in the larger fractions while the smaller size fractions are relatively unchanged. Note that the difference of volume equivalent diameter between ice crystals, which are assumed to possess irregular shape with a refractive index of 1.3–0i, and spherical particles, with a refractive index of 1.40–0i, is about 10 % (Iwasaki et al., 2007). This error is not large enough to preclude identification of cloud and/or

aerosol layers. Additional cloud layers are evident in the profile up to 8.5 km. An interesting feature to note is the strong drop in small size fractions in the layers between the clouds, possibly indicative of scavenging. The region of interest in the profile for this case study, however, is the cloud-free lowest 4.1 km.

In support of the OPC sonde launch, the CPL was operated from 18:00 UT to 23:50 UT on 19 April (Fig. 8). General results from this instrument indicate distinct horizontal banding up to ∼ 5.0 km a.m.s.l. due to stratified aerosol layers which display δ ranging from 0.05–0.09. Before 20:30 UT and above ∼ 5.0 km are found sporadic, thin cloud layers which top out at 8–12 km with cirrus. The height of the cirrus cloud top, i.e., 12.0 km a.s.l., is indicative of an elevated tropopause. After 21:00 UT this cloud can be seen to rapidly transition to a deep altostratus cloud that is optically dense enough to attenuate the laser pulses.

OPC/CPL results integration

By integrating the results from the OPC and the AFARS CPL, six distinct layers may be identified in the lowest 4.1 km, summarized in Table 1 and marked in Fig. 8. For greater clarity of vertical trends the OPC data are also presented as absolute counts by size fraction and by layer (Fig. 6), and as absolute volumes of particulate per unit volume of air, again by size fraction and by layer (Fig. 7). The first, lowest layer, extending from the surface to ∼ 330 m, is the only layer with relatively high concentrations of particulates in the largest size fractions. This is a result of urban combustion activities, including wood stove, outside wood boiler, and coal-fired power plant emissions that often lead to unhealthy $PM_{2.5}$ counts, trapped in the surface-based inversion that tends to set up in Fairbanks in the absence of strong synoptic forcing. Examination of the radiosonde launch from 12:00 UTC, 19 April (10 h earlier – not shown) confirmed the presence of a strong primary inversion from the surface to ∼ 300 m, a thin, inversion-free layer of ∼ 100 m in thickness, and a weaker, secondary inversion up to ∼ 1100 m. Because the particulate loadings for this layer are so heavily influenced by local factors, it is identified as "layer 0" and is not considered further in the same manner as the layers of atmosphere above it, which are less influenced by the surface.

A second layer (identified as layer 1), extending from 330–1080 m, may be discerned from various sources: OPC, CPL, and humidity data. The OPC showed elevated counts in the mid-sized fractions (0.5 through 3.0 µm), CPL returned higher backscatter ratios (approaching 0.1), and humidity decreased. The two largest size fractions are most strongly represented in this layer because it becomes part of the stable boundary layer during the night, entraining these size fractions (local combustion products), which then do not have enough time to settle out during the day.

A third layer (identified as layer 2) extended from 1080–2230 m. This layer is most strongly identified in the humidity trace and the CPL profile. It is the driest part of the profile – relative humidity is ∼ 20 % throughout the layer. The largest size fractions on the OPC traces are relatively high throughout the layer, with low concentrations at the top and bottom, although volumetric concentrations of small size fractions were almost double that of the large fractions. The CPL indicates this layer possesses the lowest depolarization ratios in the profile.

The next layer (identified as layer 3) extended from ∼ 2400–3020 m. This layer was characterized by strongly increasing humidity and a profile maxima for 2–5 µm size fractions in the OPC (Fig. 8), which exceeded that of the smaller size fractions by 50 %. This layer exhibited much higher depolarization ratios in the CPL profile.

Layer 4, extending from 3020–3450 m, exhibited moderate concentrations in the smallest and the ∼ 3 µm size fractions. It also possessed the highest humidity below the cloud layer. CPL depolarization remained high in this layer, although at the bottom part of the layer, depolarization was a little lower. Although overall volumetric counts were lower than observed in layer 3, the ratio of large particles to small remained high, similar to layer 3.

The final layer, layer 5, extends from 3450– ∼ 4100 m; up to the cloud base. All OPC size fractions decline in this layer, with the smallest size fractions exhibiting the sharpest decline. The ratio of large particles to small is again high in this layer. Humidity is relatively low until the cloud base, and CPL depolarization remains high. Note that, for all layers except layer 5, the size fraction ∼ 1–1.5 µm possesses the lowest concentrations. Above this layer was a layer of ice cloud.

3.4 Regional-scale climate

3.4.1 Mean patterns

The bulk of the Alaska region is situated far enough to the north to place it north of the polar jet stream in winter, and well in its path in the summer. April is a transition season – regionally, patterns typical of winter still dominate, which can include large portions of the Interior coming under the influence of a surface-based density high, upper levels dominated by a corresponding weak low, and large-scale flow patterns dominated by a jet stream flow moving along or south of the Aleutian Islands. Periods of strong southerly flow into Interior Alaska, which occur during marked departures from zonal flow, are becoming more frequent in April than in winter as the jet stream moves north.

By mid-April, the day length in Interior Alaska is exceeding 15 h with a maximum solar elevation approaching 40°. Roughly half of the days in April can expect clouds. Typically, snow is still on the ground at least through mid month. This results in the local scale near the ground remaining dominated by snow- and ice-covered surfaces which inhibit radiation-based heating and favor surface inversions, despite

Table 1. Layers present in the lowest 4.1 km of the atmosphere for the Fairbanks area, 22:00 UTC, 19 April 2008, as derived from OPC observations.

Layer	Height range (m)	Defining features				Apparent cause
		Concentration in submicron size fraction	Concentration in micron size fraction	Relative humidity	Depolarization ratio	
0	188–330		Maxima, ($0.027\,cm^3$) in the largest size fraction (see Fig. 5)	Moderate About 40 %	–	Urban combustion by products trapped by strong surface inversion.
1	330–1080	High	High	Low about 30 %	Moderate 0.05–0.1	Haze layer trapped under weaker secondary inversion.
2	1080–2230	High	Moderate	Low about 20 %	Low < 0.05	
3	2400–3020	High	High	Moderate 50–60 %	High around 0.15	Dust
4	3020–3450	Moderate	Moderate	High 60–70 %	High around 0.15	Dust
5	3450–4100	Low	Low	Variable 35–70 %	–	Cloud scavenging of aerosols.

the rapidly increasing influx of shortwave radiation. Typically, the inversion pattern transitions from a semi-permanent inversion situation in January/February, associated with the low radiation input and broken only by strong synoptic forcing, to one in which the inversion settles in overnight and is broken radiatively during the day.

3.4.2 Synoptic patterns during ARCTAS, 5–19 April 2008

The most prominent climatological feature exhibited during the timeframe of the ARCTAS experiment was the strong high pressure anomaly in the Gulf of Alaska/south Bering Sea, noted earlier. This pattern favored flow into Gulf of Alaska and the western, northern and Interior parts of Alaska in April 2008 (Fig. 9), which is not the typical pattern for April (Fig. 10). During some periods at some levels, the pressure pattern to the west of the Bering Sea was arranged such that air masses originating from the mid- and northern-Siberian regions were directed towards the Bering Sea area, and from there on into the Alaska region. The climatological mean pattern for this period does exhibit flow moving across the same region of Siberia, but the air mass is directed south-easterly, out into the Northern Pacific where, after a relatively lengthy trip, it can reach Interior Alaska from the southeast, around one of the transient low pressure systems that are frequently found in the Gulf of Alaska at this time.

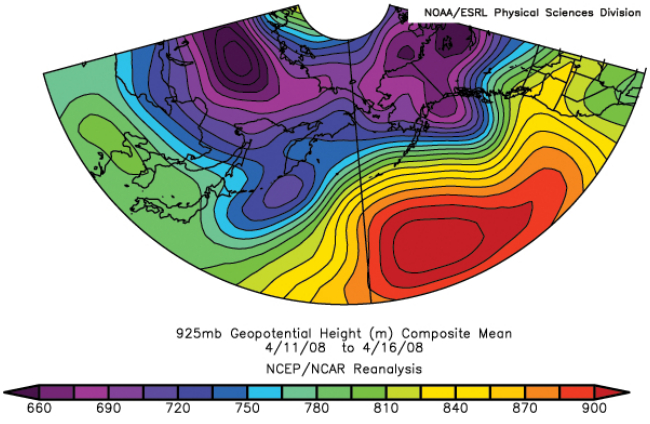

Fig. 9. Mean 925 hPa geopotential height (m) pattern, 11–16 April. The large high pressure zone south of the Aleutians pushes the Asian exit flow northwards such that it is in a position to move into the AK Interior between the mountain ranges. This represents the most favorable pathway to transfer unmodified airmasses into the Interior. This period captures the general trajectory leading to the balloonsonde launch of 19 April.

Over Interior Alaska up to ~16 April, a general pattern of weak northwesterly flow was in place. This was characterized near the surface by low moisture content and little cloud cover, with correspondingly cool temperatures in the −10 to −20 °C range. This resulted in a large diurnal

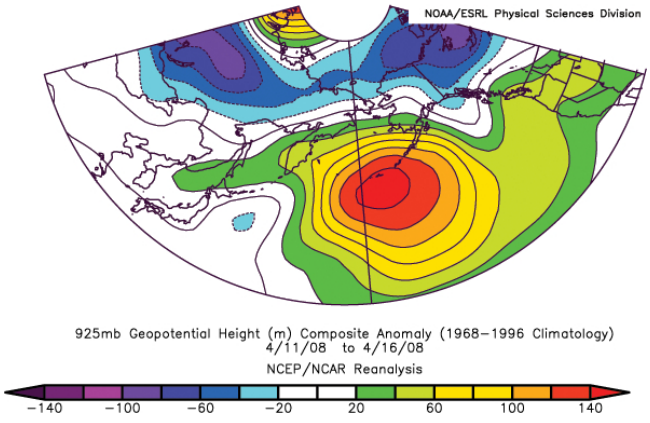

Fig. 10. Anomaly for the same date and parameter as shown in Fig. 9. The region of high pressure over the Aleutians during this period is not typical for this period.

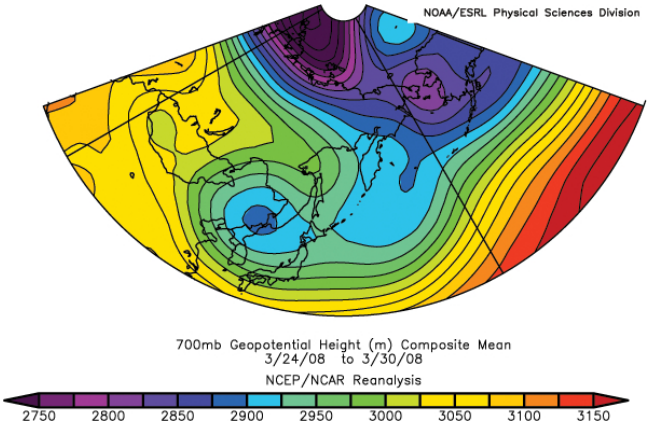

Fig. 11. Mean 700 hPa geopotential height (m) pattern, 24–30 March 2008. This represents rough synoptic flow paths leading up to the "Arctic Haze" period. Locations of the Norilsk region of Northern Russia (white dot) and the Fairbanks area (white triangle) are indicated.

variation in surface air temperature which facilitated formation of a nighttime radiation inversion of several hundred meters depth. During this time the dominant pressure pattern control was a strong area of high pressure situated over the Aleutian Islands (Fig. 10). By the second week in April, a low pressure system had approached from the southwest, moving up the east side of Kamchatka Peninsula, and displaced the high towards the east. This initiated a pattern whereby Interior Alaska was dominated by a pronounced strong, anomalous, westerly/southwesterly flow throughout the lower- to middle-levels of the atmospheric column (925 hPa, 700 hPa, 500 hPa). This brought unusually cool temperatures at the lower levels (coolest near surface, warming to neutral anomaly at ∼3000 m) and unusually warm temperatures at higher levels (warm anomaly increasing above ∼4000 m). It also caused an increase in air mass moisture content and temperatures. Cloud cover increased and surface diurnal cycling ceased. By 18 April the anomalous high pressure zone had shifted southeastwards, moving from the south Bering Sea to lie over the central Gulf of Alaska, with associated flow coming from the north Pacific over Interior Alaska. In response, temperatures at the low levels warmed to become positive anomalies.

4 Discussion

Visual inspection of the DRUM concentration time series plots, combined with the information about aerosols provided by the CPL data, suggest four distinct, multiday aerosol loading "periods": (1) an "Arctic Haze" period during the last week of March, (2) a "pristine" period during the first few days of April, (3) a "dust/smoke" period during the second week of April and (4) a "smoke-dominated" period during the third week of April.

The Drum Impactor sampler traces are the most continuous over the observation timeframe and lay the foundation for clear identification of aerosol period timing. Summary statistics for Drum results, broken out by period, are presented in Table 2. CPL profiles available during most days of the experiment exhibited backscatter distribution patterns and strengths and depolarization ratios that indicated several aerosol events during which mineral dust, smoke, or a mixture of the two was likely present. CPL measurements are in turn verified by the OPC-sonde data profiles which matched the larger particulates in dry layers with high backscatter ratios. Climatologically, indications of the general nature of departure of this period from climatology have been highlighted here, as treated in greater depth in F10. With that groundwork established, this section will lay out the synoptic progression in greater detail for each aerosol event identified in the results. This will include an integrated discussion of the events in terms of synoptic patterns, as supported by trajectory analyses.

4.1 Arctic Haze period

The synoptic pattern during the Arctic Haze period was dominated by a strong low pressure region situated over the East Siberian Sea with a trough extending to the east linking up with a secondary center of low pressure situated over the Bering Sea. This resulted in a flow pattern that passed over Northern Russia and continued east across northern Siberia, entrained around the Bering Sea low feature and finally advected over the Alaska Interior (Fig. 11). It is possible this air mass passed near enough to the Norilsk industrial region, a known Arctic Haze emission source area (Wilcox II and Cahill, 2003), to entrain aerosols. This synoptic pattern in general is not unusual for this time of year, however there were departures from climatology which took the form of a stronger and more compact low pressure feature over the East Siberian Sea. This low shifted the flow path farther to

Table 2. Summary statistics for DRUM Impactor sampled species by inferred period. Size fraction is 0.34–1.15 µm. All values are in units of mass concentration ng m^{-3}. "SD" means standard deviation. "AEU" means Average Experimental Uncertainty.

		S	K	Si	Ca	Fe
Period 1	Average	31.43	1.35	2.55	1.24	0.92
	SD	10.98	0.51	1.28	0.63	0.55
	AEU	1.66	0.07	0.23	0.07	0.05
Period 2	Average	6.87	0.23	1.24	0.32	0.61
	SD	4.27	0.12	0.49	0.08	0.27
	AEU	0.42	0.01	0.12	0.02	0.04
Period 3	Average	110.84	3.56	5.80	2.60	1.58
	SD	34.05	1.60	2.78	1.73	0.58
	AEU	5.65	0.19	0.46	0.15	0.09
Period 4	Average	144.24	6.67	7.45	0.53	1.48
	SD	80.03	4.51	2.38	0.47	0.76
	AEU	7.33	0.35	0.58	0.06	0.08

the north/northeast than would typically be observed for this period. This likely served to isolate the northern airmass, reducing contamination by smoke or dust from source regions situated farther south and resulting in a "classic" haze signature, possessing slightly elevated industrial tracers, as observed by both the CPL and the DRUM sampler (Fig. 3). The relatively weak signature observed by both ground instruments is likely due to an initial injection of a limited quantity of aerosol. Note that during this period the flow into the Alaska Interior was enhanced, both in terms of gradient (speed) and directionality, by the presence of a high pressure region in the northeastern Gulf of Alaska, which was another departure from climatology.

4.2 Pristine period

Starting 1 April and over the next few days, the strong low pressure center situated over the East Siberian Sea weakened and became more symmetric, losing the trough feature that extended to the east. At the same time a second strong low pressure center developed east of Japan and moved slowly to the north-northeast towards the Bering Sea. By 2/3 April these two features joined to form a broad zone of low pressure extending from the Kara Sea to the Bering Sea. The Bering Sea dipole possessed a deep trough extending well to the southwest, reaching Japan (Fig. 12). While the low pressure merger was happening, a strong and climatologically anomalous high pressure region developed over the central North Pacific. The net result of this pattern was the direction of flow into the Alaska Interior from the western North Pacific Ocean by way of the Alaska Range (Fig. 13). This combination meant that entrained air parcels (a) started in a relatively clean region at mid-tropospheric heights, (b) had little potential to entrain aerosols due to lack of contact with terrestrial source regions, (c) spent an extended period over the northwest Pacific Ocean, providing opportunity for aerosol loss due to settle-out and due to scavenging by wet deposition processes and (d) experienced forced orographic ascent, again allowing opportunity for precipitation scavanging. The combination of these factors and processes likely contributed to greatly reduce the aerosol loading, thus accounting for the extraordinarily clear conditions recorded by the CPL and DRUM sampler from 1 April to midday 5 April that immediately preceded the initiation of ARCTAS activity.

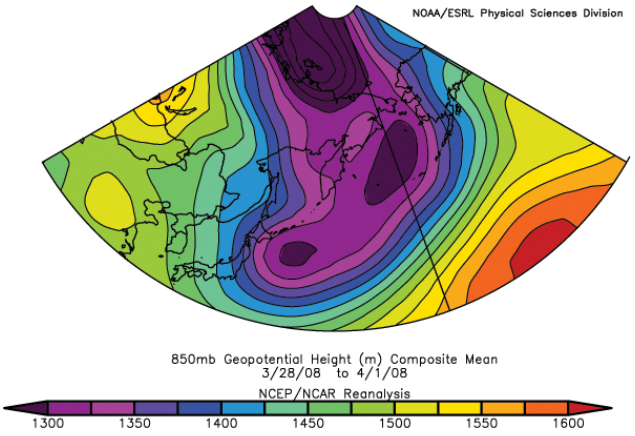

Fig. 12. Mean 850 hPa geopotential height (m) pattern, 28 March–1 April 2008. This represents rough synoptic flow paths leading up to the "Pristine" period.

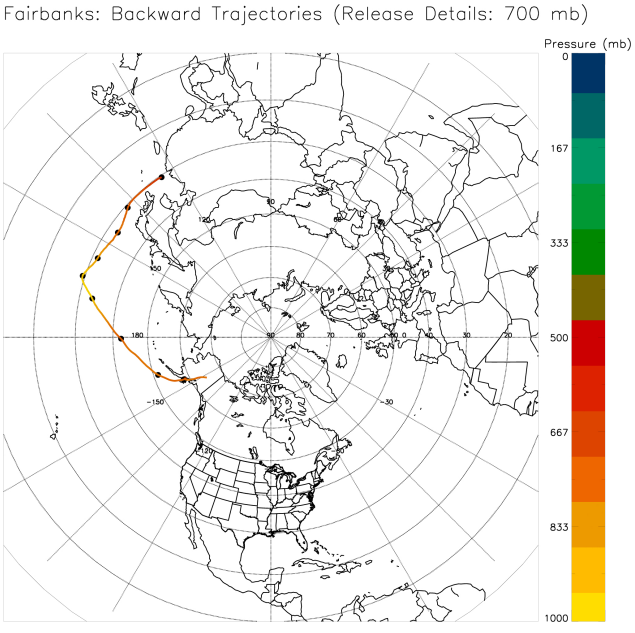

Fig. 13. FLEXPART back trajectory ending 3 April 2008 at 700 hPa over Fairbanks, Alaska. Each black dot represents one day. Elevation for all FLEXPART trajectories was determined using distinct layers observed in the lidar data.

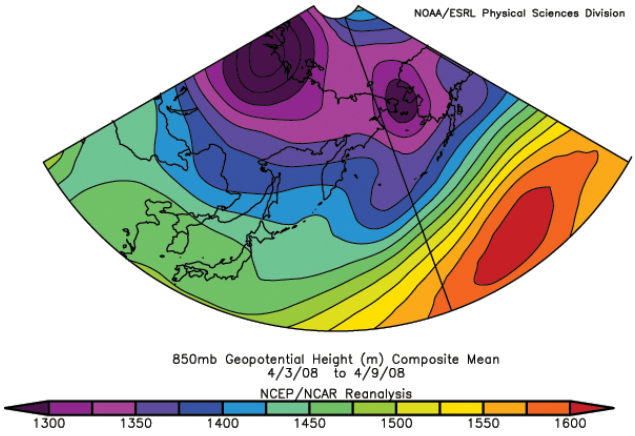

Fig. 14. Average synoptic situation, 28 March–5 April 2008. 850 hPa GPZ (m).

4.3 Smoke/dust period

A rapid transition occurred on 5 April 2008, when clean atmospheric conditions gave way to aerosol loading. This coincided with the passage of a cold front through Interior Alaska, as evidenced by data from Fairbanks Airport. Several variables exhibited rapid changes, including dry bulb temperature, which dropped from daytime highs in the 5–7 °C range to the −5–−3 °C range; dew point temperature, which dropped from −1–−4 °C to −10–−12 °C; wind speed, which rose from 0 to 6 m s^{-1}; and precipitation (light snow), which began at the same time as the other observed changes. Cloud conditions went from scattered/broken to overcast. Establishment of a large-scale flow pattern able to advect aerosols over the Alaska Interior was initiated by changes to the Bering Sea low, including a weakening of the southeast trough feature and a shift of the low to the north, over the south Chukchi Sea. A low with a trough to the south persisted over the Kara Sea. Finally, a low pressure system formed over Japan and moved slowly north northeastward towards Kamchatka, establishing a broad area of low pressure along the Asian east coast up to the Bering Sea. Combined, these features set up a flow trajectory directed initially to the southeast over the Lake Baikal/Mongolian region and then east-northeastward towards west Alaska (Fig. 14). This flow pattern represents a fairly direct pathway from north China/southern east Siberia, which was maintained over the next few days by the continued presence of the high pressure feature in the central North Pacific. Thus, in contrast to the pristine period, air masses advected over the Interior after 5 April had moved over dust and fire source regions, spent less time over the ocean and did not traverse the Alaska Range. These pathways are suggested by a pressure analysis and supported by backtrajectories (Figs. 15, 16).

Observations from CPL (Fig. 2b–d) and DRUM sampler (Fig. 3) suggest a dominant dust signature with smoke. During this period fires were burning in the Kazakhastan region

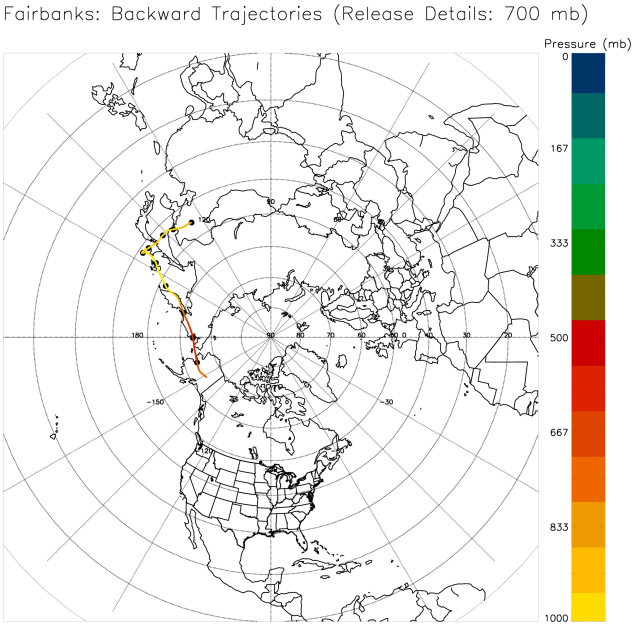

Fig. 15. FLEXPART back trajectory ending 13 April 2008 at 700 hPa over Fairbanks, Alaska. Each black dot represents one day. Large red circles indicate regions of southeast Siberian fire activity.

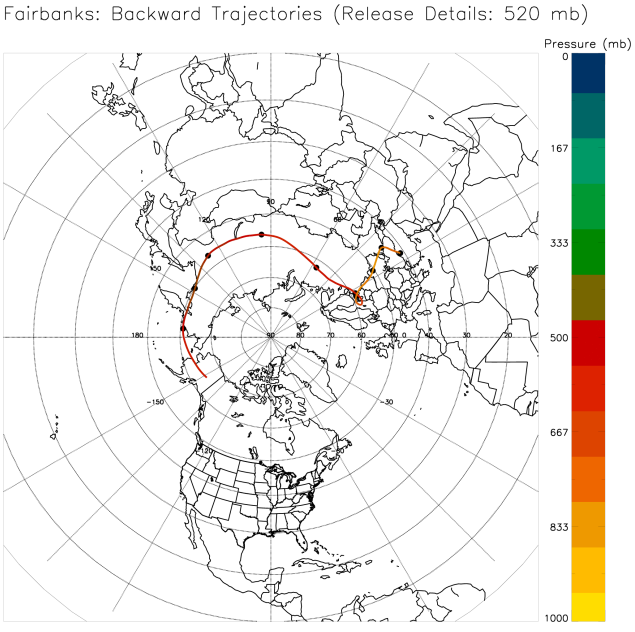

Fig. 16. FLEXPART back trajectory ending 15 April 2008 at 520 hPa over Fairbanks, Alaska. Each black dot represents one day. Large red circles indicate regions of southeast Siberian fire activity.

(agricultural) and southern Siberia, near the northern Mongolia border (boreal forest). Warneke et al. (2009) indicate the unusually early start to the fire season this represented. In late March and very early April boreal fire emissions were not well established; the predominant source was the agricultural

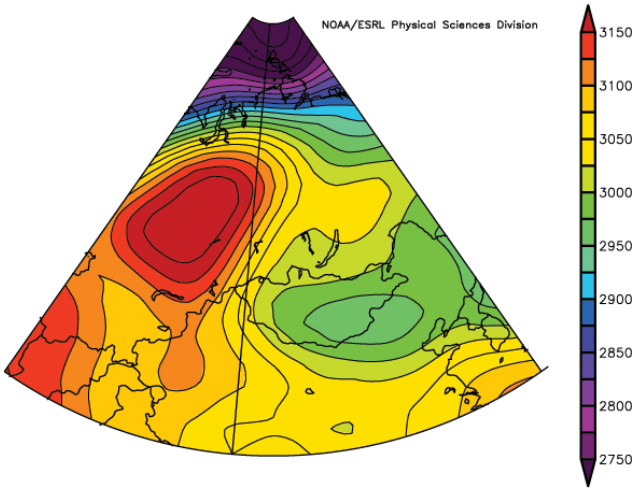

Fig. 17. Mean 700 hPa geopotential height (m) pattern, 28 March 2008. Possible Takla Makan dust-raising event. Plot spans latitudes 40–85° N and longitudes 60–130° W. Mongolia is near the center of the plot, with Lake Baikal just north of Mongolia.

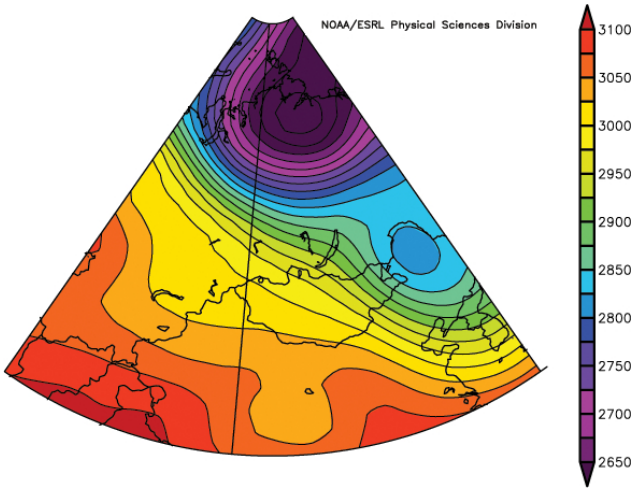

Fig. 18. Mean 700 hPa geopotential height (m) pattern, 2 April 2008. Possible Gobi dust raising event. Plot spans latitudes 40–85° N and longitudes 60–130° W. Mongolia is near the center of the plot, with Lake Baikal just north of Mongolia.

burning component. The pathway indicated in Fig. 16 would entrain smoke from this region and bring it over Alaska. The occurrence of crustal species, unlike smoke, requires a suitable synoptic event at the point of origin to loft the aerosols. Synoptic analysis suggested two possible events. The first commenced 28 March over central Asia, where a compact high pressure feature developed over eastern Kazakhstan. This established a strong pressure gradient with flow directed south across eastern Kazakhstan in the region of the Takla Makan Desert; flow then turned eastward across the northern region of China, in the vicinity of the Gobi Desert (Fig. 17). Wind speed estimates from NCEP/NCAR reanalysis exceeded 20 m s^{-1}, more than sufficient to raise dust into the atmosphere (Australian Bureau of Meteorology). The K-lifting index, a measure of convective instability, was also elevated over the Takla Makan Desert region, suggesting instability sufficient to move raised dust into the atmosphere for transport. The second event commenced 2 April. A strong pressure gradient was established across the Gobi Desert. The strong winds accompanying this event were associated with a cold front leading a cold air outbreak that pushed southeastwards through eastern Mongolia and into northern China (Fig. 18). Various authors point out that raised dust events occur every year in the Gobi and Takla Makan region during the March–May season (Lee et al., 2006; Wetzel et al., 2003; Cahill, 2003); the observation of crustal species in the aerosols reaching the Alaska Interior given favorable large-scale flow patterns is therefore not an unexpected occurrence.

4.4 Smoke period

The final period was defined by another major change in DRUM sampler species traces that occurred 17–18 April.

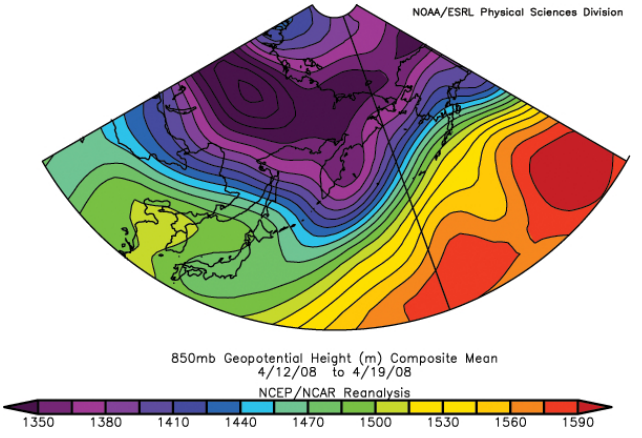

Fig. 19. Mean 850 hPa geopotential height (m) pattern, 12–19 April 2008.

The large-scale synoptic pattern was dominated by a broad region of low pressure that was established north of Mongolia and which extended well to the east, with a smaller low pressure zone over Kamchatka (Fig. 19). The high pressure over the North Pacific persisted. This established a flow pattern that could advect air directly over known fire zones in eastern Kazakastan and just south and east of Lake Baikal, and away from the desert regions farther south. Boreal forest fires by this time in April were well underway in southern Siberia (Fig. 20).

The OPC-sonde case-study ascent was conducted on 19 April (Figs. 4–7). The detailed profile loading data provided a means to verify and understand in greater detail what the CPL was recording (Fig. 8). Three main features emerged. First is the presence of the elevated large size fraction loading in the lowest levels. For level 0 this was clearly

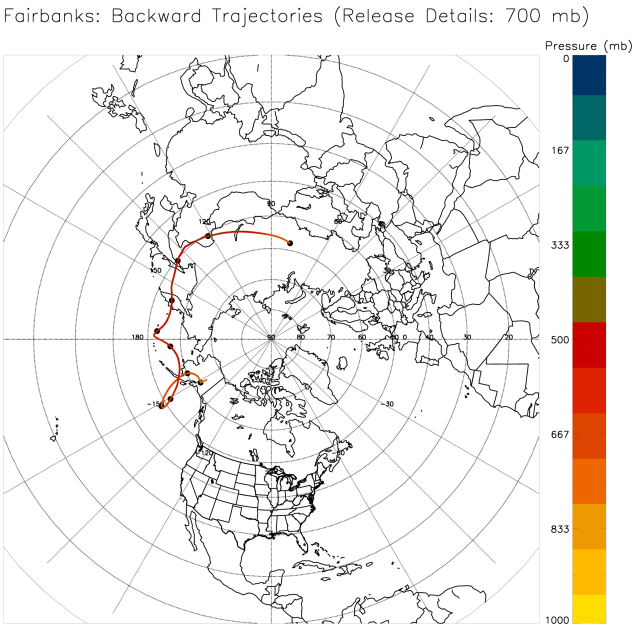

Fig. 20. FLEXPART back trajectory ending 21 April 2008 at 700 hPa over Fairbanks, Alaska. Each black dot represents one day.

associated with combustion by-products from the Fairbanks area, trapped in the continuous surface-based inversion layer that dominated this time period. The elevated large particle count for layer 1, however, reflected the higher level diurnal component of the inversion that sets up at night. Combustion particles are entrained in this layer when fully developed during the night such that, even though it decouples from the surface inversion later in the day, it still retains high loading of large particulates. The second main feature is the presence of elevated large particulate loading aloft. These are not as large as the combustion particles and are not locally derived but likely represent Asian smoke or dust that has been advected in, as suggested by the back trajectory plots. The depolarization ratios in these layers are relatively high, indicative of large particles that do not possess a surface water layer, which means either hydrophobic mineral particles from desert dust or humid smoke particles desiccated by long-range transport. Although smoke particles can give depolarization ratios as high as 8 % after high rates of drying experienced during lengthy transport, the depolarization ratio is high enough – approaching 9 % – to suggest at least an inclusion of desert dust. This is also supported by the DRUM sampler data, which exhibited a large peak in smoke species concentration on 19/20 April. The third main feature is the fact that the atmospheric constituents are arranged in discrete layers. This is also indicative of long-range transport.

5 Summary

In general, it should be pointed out that, in comparison to earlier spring-transition months (March through May) from AFARS, the ARCTAS period data seems unusual in that more dramatic and highly depolarizing aerosol episodes are lacking. This is particularly apparent because of the absence of strongly scattering aerosol layers derived from Asian dust storms (Sassen, 2005b). Forest fire smoke episodes transported from northern China and eastern Russia are also not uncommon at AFARS in spring. It is suggested that aerosols of mixed composition (haze, dust and aged smoke) and relatively small size and concentration were dominant, perhaps affected by cloud processing between the midlatitude source region and AFARS. It is also intriguing that, after the indicated onset of midlatitude mixing in mid-April, at midlevels the cirrus and other ice clouds often appear to be associated with diffuse aerosol layers. It has previously been shown from AFARS that springtime ice cloud formation can be linked the presence of midlatitude aerosols transported to the previously clean Arctic region (Sassen, 2005b).

Given that the elemental compositions observed by the DRUM sampler are consistent with known source emissions from the areas crossed by the trajectories, it appears that at least some of the upper level aerosols are being mixed downwards in the atmosphere. However, the low concentrations at ground level and the higher altitude aerosol layers observed by the CPL imply that only a small fraction of the upper-level aerosol plumes have been mixed downwards. This is consistent with the strong zone of stability in the lowest levels of the boundary layer in the Alaska Interior; on many occasions it is decoupled from the higher level atmosphere and mitigates vertical mixing.

An important aspect of this paper has been the case made for the existence of a robust mineral component in the aerosol loadings. A lot of attention has been focused on the agricultural and boreal forest fire sources by other papers resulting from the ARCTAS and corresponding NOAA ARCPAC efforts, which was a primary scientific objective for ARCTAS. However, Interior Alaska ground-based instrumental results, combined with trajectory traces and detailed central Asian synoptic assessments, do argue for the inclusion of a mineral source load in the plumes advected over this region during the second week of April 2008.

The sensitivity of Alaska atmospheric loading is apparent in the speed and extent to which the aerosol load can change as the synoptic situation evolves. The observations conducted during the time-frame of ARCTAS-A provided examples of four major loading types over Alaska: “classic” arctic haze, as defined by industrial emissions transported by a high-latitude zonal pattern; less-common pristine clear skies resulting from low pressure feature situated to the west of Alaska; dust, caused by a lifting event over Asia and favorable trajectory that included an anomalous north Pacific high that shifted the trajectory farther north and

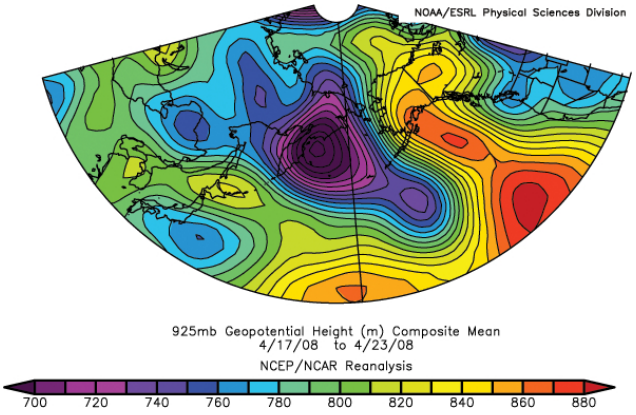

Fig. 21. Mean 925 hPa geopotential height (m) pattern, 17–23 April. This period was dominated by the incursion of a large low pressure system from the west into the Bering Sea. The anomalous high was displaced to the east. The resulting strong flow from the south brought a pronounced warming trend to the Interior. As the low moved in it displaced the main trajectory progressively farther to the south, increasing transport distance and showing up as a steady decrease in wildfire species into late April.

west to avoid the Alaska Range; and smoke, caused by a strong and early start to the Asian boreal fire season and the anomalous dust trajectory noted above. The strong loading period wound down towards the end of April as the north Pacific high was slowly replaced by the more typical expansive low-pressure system, with the trajectory directed along progressively lengthier pathways before reaching the Alaska Interior (Fig. 21). CPL and balloonsonde observations laid the groundwork for establishing likely aerosol type as dust and aged smoke; strongly layered structures also indicated lengthy transport. The surface based DRUM sampler provided details about aerosol type, again indicating their terrestrial and fire origins. Despite the activity noted during the observing campaign, the strength of the synoptic pattern anomaly suggests that the aerosol patterns observed in April of 2008 are in general not to be expected over the Alaska Interior at this time of year.

Acknowledgements. The authors wish to express their gratitude to the following agencies and projects that made this work possible: National Aeronautics and Space Agency (NASA) grant 07-ARCTAS08-0050 (G. Shaw), National Science Foundation (NSF) grants ATM-0630506 and AGS-1037000 for the AFARS research facility (K. Sassen), and National Oceanic and Atmospheric Administration (NOAA) grant NA06OAR460017 (D. Atkinson). We also wish to express our thanks to three anonymous reviewers and to the editor of ACP, Patricia Quinn, who contributed their time to improving this paper. Images provided by the NOAA/ESRL Physical Sciences Division, Boulder Colorado from their Web site at http://www.esrl.noaa.gov/psd/.

Edited by: P. Quinn

References

ACIA: Arctic Climate Impact Assessment, Cambridge University Press, 1042 pp., 2005.

Australian Bureau of Meteorology: http://reg.bom.gov.au/nsw/sevwx/facts/dust.shtml, last access: 18 February 2011.

Cahill, C. F.: Asian aerosol transport to Alaska during ACE-Asia, J. Geophys. Res., 108, 8664, doi:10.1029/2002JD003271, 2003.

Cahill, T. A., Cliff, S. S., Perry, K. D., Jimenez-Cruz, M. P., and McHugo, S. A.: Size and time resolved anthropogenic components of aerosols via synchrotron X-ray fluorescence: Application to Asian aerosol transport, EOS Transactions of the American Geophysical Union, Fall Meeting Supplement, 80, Abstract A12C-09, 1999.

Cahill, C. F., Cahill, T. A., and Perry, K. D.: The Size- and Time-Resolved Composition of Aerosols from a Sub-Boreal Forest Prescribed Burn, Atmos. Environ., 42, 7553–7559, doi:10.1016/j.atmosenv.2008.04.034, 2008.

Chiapello, I., Bergametti, G., Chatenet, B., Bousquet, P., Dulac, F., and Santos Soares, E.: Origins of African dust transported over the northeastern tropical Atlantic, J. Geophys. Res., 102, 13701–13709, 1997.

Douglas, T. A. and Sturm, M.: Arctic haze, mercury and the chemical composition of snow across northwestern Alaska, Atmos. Environ., 38, 805–820, 2004.

Fuelberg, H. E., Harrigan, D. L., and Sessions, W.: A meteorological overview of the ARCTAS 2008 mission, Atmos. Chem. Phys., 10, 817–842, doi:10.5194/acp-10-817-2010, 2010.

Halter, B. C., Harris, J. M., and Rahn, K. A.: A study of winter variability in carbon dioxide and arctic haze aerosols at Barrow, Alaska, Atmos. Environ., 12, 2033–2037, 1985.

Hayashi, M., Iwasaka, Y., Watanabe, M., Shibata, T., Fujiwara, M., Adachi, H., Sakai, T., Nagatani, M., Gernandt, H., Neuber, R., and Tsuchiya, M.: Size and Number Concentration of Liquid PSCs: Balloon-Borne Measurements at Ny-Alesund, Norway in Winter of 1994/95, J. Meteorol. Soc. Jpn., 76, 549–560, 1998.

Haywood, J. and Boucher, O.: Estimates of the Direct and Indirect Radiative Forcing due to Tropospheric Aerosols: A Review, Rev. Geophys., 38, 513–543, 2000.

Iino, N., Kinoshita, K., Tupper, A. C., and Yano, T.: Detection of Asian dust aerosols using meteorological satellite data and suspended particulate matter concentrations, Atmos. Environ., 38, 6999–7008, 2004.

Iwasaki, S., Maruyama, K., Hayashi, M., Ogino, S.-Y., Ishimoto, H., Tachibana, Y., Shimizu, A., Matsui, I., Sugimoto, N., Yamashita, K., Saga, K., Iwamoto, K., Kamiakito, Y., Chabangborn, A., Thana, B., Hashizume, M., Koike, T., and Oki, T.: Characteristics of aerosol and cloud particle size distributions in the tropical tropopause layer measured with optical particle counter and lidar, Atmos. Chem. Phys., 7, 3507–3518, doi:10.5194/acp-7-3507-2007, 2007.

Jacob, D. J., Crawford, J. H., Maring, H., Clarke, A. D., Dibb, J. E., Emmons, L. K., Ferrare, R. A., Hostetler, C. A., Russell, P. B., Singh, H. B., Thompson, A. M., Shaw, G. E., McCauley, E., Pederson, J. R., and Fisher, J. A.: The Arctic Research of the Composition of the Troposphere from Aircraft and Satellites (ARCTAS) mission: design, execution, and first results, Atmos. Chem. Phys., 10, 5191–5212, doi:10.5194/acp-10-5191-2010, 2010.

Kalnay, E., Kanamitsu, M., Kistler, R., Collins, W., Deaven, D., Gandin, L., Iredell, M., Saha, S., White, G., Woollen, J., Zhu, Y.,

Leetmaa, A., Reynolds, R., Chelliah, M., Ebisuzaki, W., Higgins, W., Janowiak, J., Mo, K. C., Ropelewski, C., Wang, J., Jenne, R., and Joseph, D.: The 1996 NCEP/NCAR 40-Year Reanalysis Project, B. Am. Meteorol. Soc., 437–471, 1996.

Lee, H. N., Igarashi, Y., Chiba, M., Aoyama, M., Hirose, K., and Tanaka, T.: Global Model Simulations of the Transport of Asian and Sahara Dust: Total Deposition of Dust Mass in Japan, Water Air Soil Pollut., 169, 137–166, 2006.

Malm, W. C., Sisler, J. F., Huffman, D., Eldred, R. A., and Cahill, T. A.: Spatial seasonal trends in particle concentration and optical extinction in the United States, J. Geophys. Res., 99, 22357–22368, 1994.

Mariano, G. L., Lopes, F. J. S., Jorge, M. P. P. M., and Landulfo, E.: Assessment of biomass burnings activity with the synergy of sunphotometric and LIDAR measurements in São Paulo, Brazil, Atmos. Res., 98, 486–499, doi:10.1016/j.atmosres.2010.08.025, 2010.

Mishchenko, M. I. and Sassen, K.: Depolarization of lidar returns by small ice crystals: An application to contrails, Geophys. Res. Lett., 25, 309–312, 1998.

Müller, D., Mattis, I., Wandinger, U., Ansmann, A., Althausen, D., and Stohl, A.: Raman lidar observation of aged Siberian and Canadian forest fire smoke in the free troposphere over Germany in 2003: Microphysical particle characterization, J. Geophys. Res., 110, D17201, doi:10.1029/2004JD005756, 2005.

Murayama, T., Müller, D., Wada, K., Shimizu, A., Sekiguchi, M., and Tsukamoto, T.: Characterization of Asian dust and Siberian smoke with multi-wavelength Raman lidar over Tokyo, Japan in spring 2003, Geophys. Res. Lett., 31, L23103, doi:10.1029/2004GL021105, 2004.

Polissar, A. V., Hopke, P. K., Paatero, P., Kaufmann, Y. J., Hall, D. K., Bodhaine, B. A., Dutton, E. G., and Harris, J. M.: The aerosol at Barrow, Alaska: long-term trends and source locations, Atmos. Environ., 33, 2441–2458, 1999.

Raabe, O. G., Braaten, D. A., Axelbaum, R. L., Teague, S. V., and Cahill, T. A.: Calibration Studies of the Drum Impactor, J. Aerosol Sci., 19, 183–195, 1988.

Sassen, K.: Lidar Backscatter Depolarization Technique for Cloud and Aerosol Research, in: Light Scattering by Nonspherical Particles: Theory, Measurements, and Geophysical Applications, edited by: Mishchenko, M. L., Hovenier, J. W., and Travis, L. D., Academic Press, 393–416, ISBN 0-12-498660-9, 2000.

Sassen, K.: Polarization in Lidar, in: Lidar, edited by: Weitkamp, C., Springer Press, Berlin, 19–42, 2005a.

Sassen, K.: Dusty ice clouds over Alaska, Nature, 434, p. 456, 2005b.

Sassen, K.: Identifying Atmospheric Aerosols with Polarization Lidar, in: Advanced Environmental Monitoring,, edited by: Kim, Y. J. and Platt, U., Springer-Verlag, Berlin, 136–142, 2008.

Sassen, K. and Khvorostyanov, V. I.: Cloud effects from boreal forest fire smoke: Evidence for ice nucleation from polarization lidar data and cloud model simulations, Environ. Res. Lett., 3, 025006, doi:10.1088/1748-9326/3/2/025006, 2008.

Sassen, K., Zhao, H., and Yu, B.-K.: Backscatter laser depolarization studies of simulated stratospheric aerosols: Crystallized sulfuric acid droplets, Appl. Opt., 28, 3024–3029, 1989.

Seinfeld, J. H. and Pandis, S. N.: Atmospheric Chemistry and Physics – From Air Pollution to Climate Change (2nd Edn.), John Wiley & Sons, 2006.

Shaw, G. E.: The Arctic Haze Phenomenon, B. Am. Meteorol. Soc., 76, 2403–2413, 1995.

Stohl, A., Berg, T., Burkhart, J. F., Fj´æraa, A. M., Forster, C., Herber, A., Hov, Ø., Lunder, C., McMillan, W. W., Oltmans, S., Shiobara, M., Simpson, D., Solberg, S., Stebel, K., Ström, J., Tørseth, K., Treffeisen, R., Virkkunen, K., and Yttri, K. E.: Arctic smoke – record high air pollution levels in the European Arctic due to agricultural fires in Eastern Europe in spring 2006, Atmos. Chem. Phys., 7, 511–534, doi:10.5194/acp-7-511-2007, 2007.

Warneke, C., Bahreini, R., Brioude, J., Brock, C. A., de Gouw, J. A., Fahey, D. W., Froyd, K. D., Holloway, J. S., Middlebrook, A., Miller, L., Montzka, S., Murphy, D. M., Peischl, J., Ryerson, T. B., Schwarz, J. P., Spackman, J. R., and Veres, P.: Biomass burning in Siberia and Kazakhstan as an important source for haze over the Alaskan Arctic in April 2008, Geophys. Res. Lett., 36, L02813, doi:10.1029/2008GL036194, 2009.

Wetzel, M. A., Shaw, G. E., Slusser, J. R., Borys, R. A., and Cahill, C. F.: Physical, Chemical and Ultraviolet Radiative Characteristics of Aerosol in Central Alaska, J. Geophys. Res., 108, 4418, doi:10.1029/2002JD003208, 2003.

Wilcox II, W. J. and Cahill, C. F.: Regional Haze Trends in Alaska: Implications for Protected Class I Visibility Areas, EM, December 2003, 34–39, 2003.

Yamasoea, M. A., Artaxoa, P., Miguel, A. H., and Allen, A. G.: Chemical composition of aerosol particles from direct emissions of vegetation fires in the Amazon Basin: water-soluble species and trace elements, Atmos. Environ., 34, 1641–1653, 2000.